

Magnetic interactions and excitations in SrMnSb₂

Zhenhua Ning,¹ Bing Li,¹ Arnab Banerjee,² Victor Fanelli,³ Doug Abernathy,³
Yong Liu,¹ Benjamin G Ueland,¹ Robert J. McQueeney,¹ and Liqin Ke¹

¹*Ames National Laboratory, U.S. Department of Energy, Ames, Iowa 50011*

²*Department of Physics and Astronomy, Purdue University, West Lafayette, IN 47906*

³*Neutron Scattering Division, Oak Ridge National Laboratory, Oak Ridge, TN, 37831*

(Dated: January 30, 2024)

The magnetic interactions in the antiferromagnetic (AFM) Dirac semimetal candidate SrMnSb₂ are investigated using *ab initio* linear response theory and inelastic neutron scattering (INS). Our calculations reveal that the first two nearest in-plane couplings (J_1 and J_2) are both AFM in nature, indicating a significant degree of spin frustration, which aligns with experimental observations. The orbital resolution of exchange interactions shows that J_1 and J_2 are dominated by direct and superexchange, respectively. In a broader context, a rigid-band model suggests that electron doping fills the minority spin channel and results in a decrease in the AFM coupling strength for both J_1 and J_2 . To better compare with INS experiments, we calculate the spin wave spectra within a linear spin wave theory framework, utilizing the computed exchange parameters. The calculated spin wave spectra exhibit overall good agreement with measurements from INS experiments, although with a larger magnon bandwidth. Introducing additional electron correlation within the Mn-3d orbitals can promote electron localization and reduce the magnetic coupling, further improving the agreement with experiments.

I. INTRODUCTION

Transition-metal dichalcogenides have the potential for intertwined charge, structural, and magnetic states [1]. In particular, the AMnX₂ (112), $A = \text{Ca, Sr, Ba, Eu, or Yb}$ and $X = \text{Sb or Bi}$, have generated intense contemporary interest because they exhibit perfect or slightly-distorted square magnetic Mn layers predicted to support Dirac or Weyl fermions [2–6]. The coupling of magnetic order or fluctuations to such topological quasiparticles is compelling as magnetic control may allow for tuning of topological properties. Thus, understanding the basic magnetic interactions in the 112 compounds is important.

The Dirac semimetal candidate SrMnSb₂ features a slightly-distorted tetragonal structure and exhibits C-type antiferromagnetic (AFM) ordering, as shown in Figs. 1(a) and 1(b). The C-type order consists of Néel-type AFM order within the slightly-distorted square Mn sublattices and ferromagnetic (FM) along the out-of-plane direction between them. The magnetic interactions and excitations of this compound have been studied using a combination of inelastic neutron scattering (INS) and density functional theory (DFT) [7]. The study considered the nearest-neighbor (NN) exchange coupling parameter J_1 , obtained from total energy mapping of various magnetic configurations. However, due to the semi-metallic nature of SrMnSb₂, it is reasonable to expect that the magnetic coupling extends to further neighbors.

To provide a more comprehensive picture, more recent work on various systems has expanded to the minimalistic Heisenberg J_1 - J_2 model [8, 9], which factors in the next-nearest-neighbor (NNN) coupling J_2 . This model offers an elegant and straightforward framework for interpreting various spin configurations resulting from the competition between J_1 and J_2 , taking into account their relative amplitudes and signs. Experimentally, valuable

information about the values of SJ and the ratio of J_1/J_2 can be obtained through INS. However, further theoretical investigation is desirable, as it can offer a microscopic understanding of these interactions and guide the manipulation of J_{ij} , where J_{ij} is the parameter corresponding to the exchange coupling between sites i and j , to either alleviate spin frustration and tune magnetic order, or promote spin frustration and quantum spin fluctuations that can mediate electronic pairing.

Ab initio estimations of exchange parameters can be performed using different methods, including total energy mapping and linear response theory [10, 11]. The total-energy-mapping method is widely employed due to its simplicity. For isotropic exchanges, the total energies of various collinear spin configurations are often calculated in first-principles methods and mapped onto a model spin Hamiltonian. For relativistic-effect-originated exchanges, such as anisotropic exchange or the Dzyaloshinskii-Moriya interaction, spin-orbit coupling needs to be included in *ab initio* calculations, and non-collinear spin configurations may need to be considered. However, the mapping method has limitations in scenarios involving substantial spin fluctuations and can be non-unique due to the dependence on assumed model Hamiltonians. Its applicability diminishes when the variability of spin moments across different configurations, particularly in metallic compounds, becomes significant.

On the other hand, linear response theory evaluates the energy variations resulting from infinitesimal spin rotations away from the ground state. It is more computationally demanding but, in principle, more suitable for the calculation of low-temperature spin wave excitations, which can be regarded as a small perturbation to the ground state. The linear response method is also easily extensible to beyond-DFT methods that may be challenging to access the total energy, such as many-body

perturbation-theory-based GW methods [12], to better describe electronic structures and magnetic interactions in various materials [11, 13, 14]. Finally, the linear response method allows for easy resolution of pairwise interactions into orbitals and band-filling effects, revealing the microscopic origin of these exchange couplings and providing guidance for bandstructure engineering using doping and pressure.

Here, we apply linear response theory to investigate the magnetic interactions and excitations in SrMnSb₂. We calculate and resolve exchange couplings, gaining insight into the microscopic origin of the magnetism. Using the obtained exchange parameters, we calculate the spin-wave spectra via linear spin-wave theory (LSWT) and compare them with INS measurements. This comparison confirms the substantial magnetic frustration existing in the Mn layers. The linear-response results allow a discussion of how to tune the magnetic frustration by carrier doping.

II. COMPUTATIONAL AND EXPERIMENTAL METHODS

We first construct the real-space scalar-relativistic tight-binding (TB) Hamiltonian using the maximally localized Wannier functions (MLWFs) method [15–17]. The reciprocal-space Hamiltonian $H(\mathbf{k})$ is obtained through Fourier transform. To better address the potential influences from the slightly-distorted tetragonal structure, we symmetrize the TB Hamiltonian to ensure that the orthorhombic crystal symmetry is rigorously satisfied. Afterward, the corresponding Green's function $G(\mathbf{k}, \omega)$ is constructed for use in the linear response approach, as implemented in our recently developed TB Green's function code [18], to calculate the exchange couplings. Finally, with the exchange parameters in hand, we proceed to construct spin-wave spectra using a linear spin-wave (SW) method.

A. Crystal structure

SrMnSb₂ crystallizes in the orthorhombic *Pnma* (space group no.62) structure, as shown in Fig. 1(a), with lattice parameters $a = 23.19 \text{ \AA}$, $b = 4.42 \text{ \AA}$, and $c = 4.46 \text{ \AA}$ [19]. All atoms occupy different sets of 4c (*m.*) sites. For convenience in discussing the Mn-3d orbital contributions to the magnetic properties, we show the longest lattice vector \mathbf{a} along the \hat{z} direction, so the magnetic Mn layers are in the xy (\mathbf{bc}) basal plane. The primitive cell contains four formula units, and the \mathbf{bc} -basal plane is slightly distorted, resulting in the NNN exchange coupling J_2 becoming anisotropic with respect to the \hat{x} (\mathbf{b}) and \hat{y} (\mathbf{c}) directions, J_{2b} and J_{2c} . The Sr atoms are relatively weakly bonded to the Sb1 atoms and staggered above and below the Sb1 layer, forming the rhombus nets. Mn atoms form MnSb₄ tetrahedra

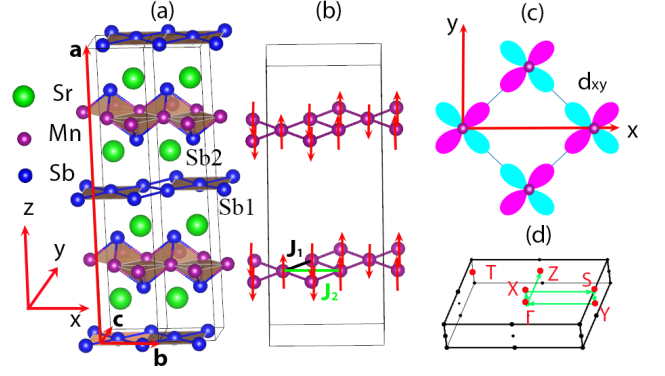


FIG. 1. Crystal structure and corresponding Brillouin zone of SrMnSb₂. (a) Schematic representation of the crystal structure of SrMnSb₂. The primitive unit cell is doubled along the \mathbf{b} direction to better illustrate the Mn grid. Sr, Mn, and Sb atoms are represented by green, purple, and blue spheres, respectively. The lattice vectors \mathbf{a} , \mathbf{b} , and \mathbf{c} are highlighted in red. For convenience in discussing the orbital contributions to exchange coupling, we align the longest lattice vector \mathbf{a} along the \hat{z} direction, and the nearly-square Mn sublattice is on the \mathbf{bc} -basal plane, or equivalently, the xy -plane. (b) Mn atoms are arranged in a rhombus net with C-type AFM order, with the NN and NNN couplings J_1 and J_2 marked. (c) Top view of d_{xy} orbitals for the Mn net shown in (b). (d) First Brillouin zone of SrMnSb₂ with high-symmetry k points marked by red dots and k path marked by green arrows.

with neighboring Sb2 atoms.

The magnetic Mn sublattice of the C-type AFM ground state is shown in Figs.1(b) and 1(c), with Mn- d_{xy} orbitals pointing along the NN direction. Figure 1(d) shows the first Brillouin zone (BZ) and special k points. Due to the large separation between Mn layers, the super-superexchange between Mn layers is much weaker than the intralayer coupling, similar to magnetic topological insulator MnBi₂Te₄ [20]. Such quasi-2D magnetic structures generally require beyond-mean-field approaches to estimate T_N [21]. Experimental lattice constants and atomic position parameters [19] are used for all calculations in this work.

B. DFT details and TB Hamiltonian symmetrization

DFT calculations are performed using the generalized-gradient approximation (GGA) with the Perdew-Burke-Ernzerhof exchange-correlation parametrization [22] and the projector augmented wave approach [23, 24] as implemented in the Vienna *ab initio* simulation package (VASP). To facilitate our subsequent analyses, we construct the MLWFs through a postprocessing procedure [15–17], as implemented in WANNIER90 [25], using the output of the self-consistent scalar-relativistic DFT calculation. In total, the TB basis comprises 44 MLWFs,

encompassing $3d$ orbitals for four Mn atoms and $5p$ orbitals for eight Sb atoms in the unit cell. To minimize the spread functional for entangled energy bands, we adopt a two-step procedure [16]. For each spin channel, a real-space Hamiltonian $H(\mathbf{R})$ with dimensions 44×44 is constructed to accurately represent the band structures in a specified “frozen” energy window. The energy bands are recalculated within TB to ensure that DFT bands can be accurately reproduced before further magnetic property calculations.

The process of wannierization for DFT bands may not always preserve the symmetry of wavefunctions and orbital characteristics. As we are also interested in understanding the potential impacts of the slightly-distorted square Mn grid on exchange couplings, we symmetrize the Hamiltonian accordingly using

$$H_{ij,\sigma}^{\text{sym}} = \frac{1}{|\mathcal{G}_H|} \sum_{\mathcal{R} \in \mathcal{G}_H} \mathcal{R} H_{ij,\sigma} \mathcal{R}^\dagger, \quad (1)$$

where \mathcal{R} represents symmetry operations within the subgroup \mathcal{G}_H of the Hamiltonian. A detailed implementation of Hamiltonian symmetrization can be found in Appendix A.

Before delving into magnetic properties calculations, we ensure alignment between the band structures generated by DFT and those produced by the symmetrized TB Hamiltonian:

$$H_{ij}^\sigma(\mathbf{k}) = - \sum_{\mathbf{R}} H_{ij}^\sigma(\mathbf{R}) e^{-i\mathbf{k} \cdot \mathbf{R}}, \quad (2)$$

where \mathbf{R} denotes primitive translation vectors, and σ represents spin channels.

C. Exchange couplings, spin wave and critical temperature

The static linear response method with the long-wave approximation [10], based on Green’s function technique, has long been developed to calculate exchange couplings as defined in a Heisenberg-type Hamiltonian:

$$H = - \sum_{i \neq j} J_{ij}^e \hat{\mathbf{e}}_i \cdot \hat{\mathbf{e}}_j, \quad (3)$$

Here, J_{ij}^e is the isotropic exchange interaction parameter between sites i and j , and $\hat{\mathbf{e}}_i$ is the unit vector pointing along the direction of the local spin moment at site i in the reference spin configuration. The early implementations were done in local-basis DFT methods, such as the linear muffin-tin orbital Green’s function method [26], often involving the atomic sphere approximation (ASA). The highly-efficient implementation in ASA methods has been used to describe [27, 28] or predict [29] magnetic interactions in various systems and has achieved great success, especially for close-packed structures. More accurate full-potential methods have also been implemented to evaluate J_{ij} from the inverse static transverse susceptibilities, using the rigid-spin approximation that projects susceptibility onto the spin density of the magnetic sites [11, 14, 30]. Finally, modern plane-wave-based DFT methods have often been interfaced with the ML-WFs method to generate realistic TB Hamiltonians that accurately describe the band structures near the Fermi level for various systems. This also provides an attractive approach to evaluate and analyze band structures and various other properties [31–33], with both speed and accuracy.

We carry out the linear response calculations using our recently-developed TB code, which has been employed to efficiently analyze band structures [34, 35], Fermi surface [36], and magnetic anisotropy [18]. Starting from the TB Hamiltonian, we construct intersite Green’s function $G_{ij}^\sigma(\mathbf{k})$ on a $16 \times 16 \times 4$ k mesh to compute the exchange parameters $J_{ij}^e(\mathbf{q})$. The real-space exchange constants $J_{ij}^e(\mathbf{R})$ are then obtained through a subsequent Fourier transformation. Their orbital-resolved components $J_{ij,m}^e$ are defined by

$$J_{ij,m}^e(\mathbf{q}) = -\frac{1}{4\pi} \Im \int_{-\infty}^{\epsilon_F} d\epsilon \int d\mathbf{k} \sum_{m'm''m'''} \Delta_i^{mm'}(\mathbf{k}) G_{ij,\downarrow}^{m'm''}(\mathbf{k}) \Delta_j^{m''m'''}(\mathbf{k}') G_{ji,\uparrow}^{m'''m}(\mathbf{k}'), \quad (4)$$

where $\mathbf{q} = \mathbf{k}' - \mathbf{k}$ and the matrix $\Delta_i(\mathbf{k}) = H_{ii}^\uparrow(\mathbf{k}) - H_{ii}^\downarrow(\mathbf{k})$.

For clarity and to facilitate comparison with conventions used in the neutron scattering community, we rewrite the spin Hamiltonian in terms of the spin vector

S as follows:

$$H = \sum_{i < j} J_{ij}^N \mathbf{S}_i \cdot \mathbf{S}_j, \quad (5)$$

where

$$J_{ij}^N = -\frac{8}{\mathbf{m}_i \mathbf{m}_j} J_{ij}^e. \quad (6)$$

Here, $\mathbf{m}_i = 2\mathbf{S}_i$ is the magnetic moment (with sign) on site i . A positive (negative) J_{ij}^N indicates AFM (FM) coupling. In contrast to J_{ij}^N , J_{ij}^e is defined with respect to the given spin configuration, and a positive (negative) J_{ij}^e indicates that the given ordering of the corresponding pair is stable (frustrated). All J_{ij} discussed hereafter, unless specified, refer to J_{ij}^N .

With the *ab initio* exchange parameters obtained, the spin wave spectra can be calculated by solving the equation of motion method or through the bosonization of the spin Hamiltonian with Holstein-Primakoff [37] or other transformations that typically retain the two-boson terms in LSWT [38]. In the latter approach, higher-order four-boson terms can be included [21] to account for magnon-magnon interactions at finite temperatures. The Néel temperature can be estimated, within the mean-field approximation, as $T_N = \frac{2}{3}J_0^e$, where $J_0^e = \sum_i J_{0i}^e$. The mean-field approximation tends to overstate the critical temperature, especially in quasi-2D magnetic structures with very weak interlayer coupling.

D. INS experiment and analysis

The INS experiment was conducted on the wide angular-range chopper spectrometer (ARCS) [39] at the Spallation Neutron Source at Oak Ridge National Laboratory. For this experiment, 19 pieces of single-crystals with a total mass of 386 mg were co-aligned. Using an optical microscope with polarized light, twin domains due to the slightly orthorhombic unit cell, each rotated by 90° with respect to the other, were observed on single-crystal pieces. Therefore single-crystals were treated as pseudo-tetragonal while using our x-ray Laue camera to make the co-alignment. The horizontal scattering plane was defined as (H, K, L) , where the momentum transfer $\mathbf{Q} = (2\pi/b)K\hat{\mathbf{i}} + (2\pi/c)L\hat{\mathbf{j}} + (2\pi/a)H\hat{\mathbf{k}}$. The rocking scans of the co-aligned assembly yielded full widths at half maximum of 3 degrees. The measurements were performed with the incident neutron energy of $E_i = 50$ meV or 125 meV at a temperature of $T = 20$ K.

To analyze the INS data, we made least-squares fits and simulations utilizing the software package PYLISW [40].

III. RESULTS AND DISCUSSIONS

A. Electronic band structure and magnetization for SrMnSb₂

We first calculate the total energies of SrMnSb₂ with various magnetic orderings, including FM, as well as

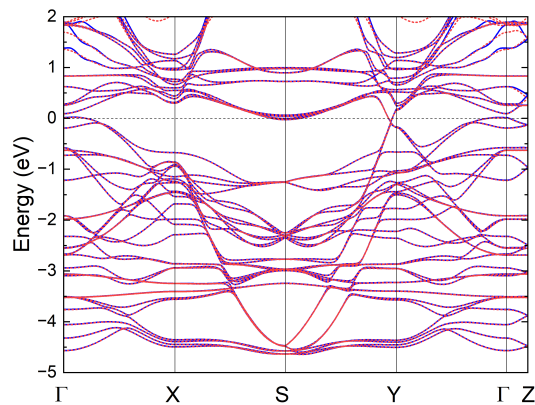


FIG. 2. Band structure of SrMnSb₂ calculated using tight-binding (TB) and density functional theory (DFT). The TB bands are shown as solid blue lines and the DFT bands are shown as red dots. The horizontal dashed line indicates the Fermi level.

C-, G-, A-, and Stripe-type AFM configurations. Our calculations yield a Mn on-site magnetic moment of $3.81 \mu_B/\text{Mn}$ and confirm that the C-type AFM ordering has the lowest energy among all the configurations, consistent with both experimental observations and prior computational studies [7, 41–43].

The MLWFs included in the TB Hamiltonian are determined by investigating the bandstructure characters near the Fermi level in DFT. According to DFT calculations, the Mn-3*d* states dominate in the vicinity of the Fermi energy and in the energy range of -4.0 – 2.5 eV in the majority spin channel and 0 – 1.5 eV in the minority spin channel, revealing a spin splitting of about 3.8 eV. The more dispersive Sb-5*p* states also contribute to the bandstructure in the relevant energy window. On the other hand, the unoccupied Sr-4*d* states are located approximately 3 eV above the Fermi energy and can be neglected. Consequently, the TB basis consisting of Mn-3*d* and Sb-5*p* Wannier orbitals provides a reasonable description of the electronic structure in the vicinity of E_F .

As noted above, the Wannierization procedure, in general, may not preserve the system's symmetry. The basis Wannier functions might center at positions that deviate from the atomic centers, and their orbital characteristics may not be preserved. We observe that the non-symmetrized TB Hamiltonian, based on MLWFs, slightly breaks symmetry of SrMnSb₂. Therefore, we symmetrize the TB Hamiltonian using Eq. (1) before conducting magnetic property calculations.

Figure 2 compares the electronic band structures along the k -path Γ -X-S-Y- Γ -Z, calculated using the symmetrized TB method (in blue) and DFT (in red). The excellent agreement in this energy window allows for a reasonable description of magnetic properties using the TB Hamiltonian. Furthermore, the on-site Mn spin moments, calculated using the symmetrized TB Hamiltonian, amount to $3.76 \mu_B/\text{Mn}$, agreeing well with DFT

and experimental results [7, 42].

B. Magnetic interactions: Orbital contributions and Bandfilling effects

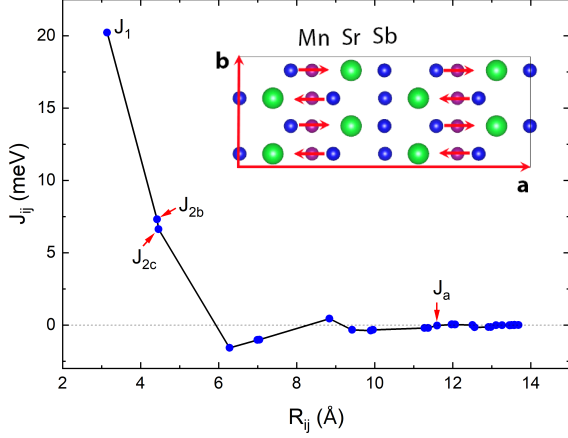


FIG. 3. Real-space magnetic exchange parameters J_{ij} in SrMnSb_2 as a function of neighbor distance R_{ij} . The spin configuration of the C-type magnetic ground state is shown in the inset.

Figure 3 presents the real-space magnetic exchange parameters J_{ij} as a function of Mn-Mn distance R_{ij} obtained from the linear-response method. It is noteworthy that J_{ij} is dominated by NN exchange coupling J_1 and NNN exchange coupling J_2 and experiences a rapid decay as R_{ij} increases, becoming negligible after $R_{ij} = 8 \text{ \AA}$. Both J_1 and J_2 exhibit positive values, indicating AFM interactions for both NN and NNN. The amplitude of J_2 is about 1/3 of J_1 . Furthermore, due to the slight structural distortion, J_2 splits into two inequivalent couplings, J_{2b} and J_{2c} , with $R_{ij} = 4.42 \text{ \AA}$ and 4.46 \AA , respectively. Considering that C-type configuration displays Néel-type in-plane AFM ordering, with AFM NN and FM NNN ordering within the **bc** basal plane, the sizable AFM J_2 suggests magnetic frustration.

TABLE I. Pairwise exchange parameters J_{ij} for the NN and NNN exchange parameters J_1 , J_{2b} , and J_{2c} (meV) and their contributions from Mn-3d orbitals in SrMnSb_2 . As shown in Fig. 1(a), we align the the Mn **bc** basal plane in the *xy* Cartesian plane for the convenience of orbital-contribution discussion.

J_{ij} No.	R_{ij}	xy	yz	z^2	xz	$x^2 - y^2$	Total	SJ	INS	
J_1	4	3.14	8.36	3.68	3.18	3.85	1.60	20.67	38.86	27.51(6)
J_{2b}	2	4.42	0.77	1.47	0.84	4.19	0.21	7.48	14.06	11.19(5)
J_{2c}	2	4.46	0.83	3.51	0.77	1.49	0.17	6.77	12.73	7.78(9)

The values of J_1 , J_{2b} , and J_{2c} , along with their Mn-3d orbital contributions, are provided in Table I. The dominant contribution to the AFM coupling J_1 originates

from the d_{xy} orbital, which directly connects two NN Mn sites, as visually depicted in Fig. 1(c). Other d orbitals make smaller AFM contributions to J_1 . Additionally, the d_{yz} and d_{xz} orbitals exhibit slightly different contributions, reflecting the small distortion in the Mn basal plane.

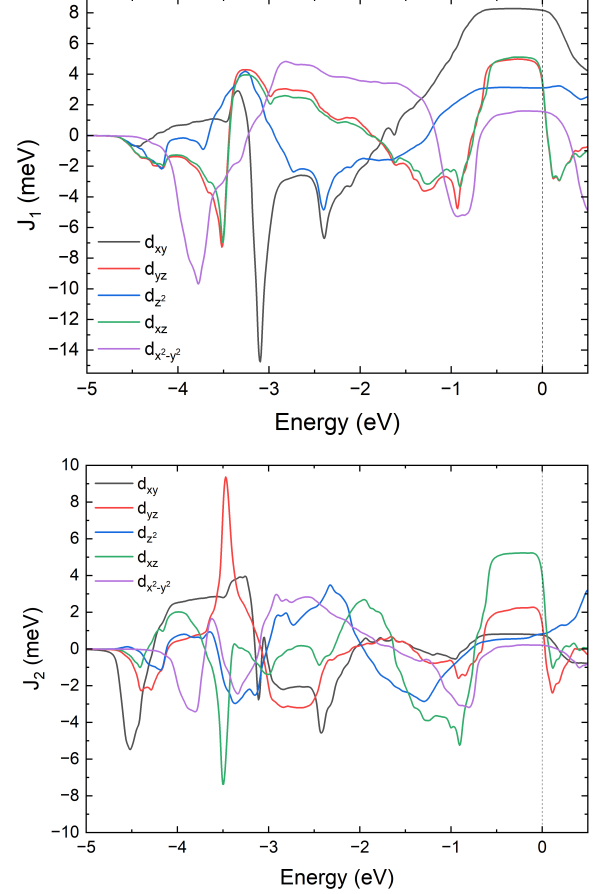


FIG. 4. Orbital-resolved exchange parameters of SrMnSb_2 are plotted with color weights, with black identifying the Mn- d_{xy} state, blue the Mn- d_{3z^2-1} states, red the Mn- d_{yz} states, green the Mn- d_{xz} state and purple the Mn- $d_{x^2-y^2}$. The horizontal zero is the Fermi level.

J_{2b} and J_{2c} are oriented along the **b** (\hat{x}) and **c** (\hat{y}) directions, respectively. Consequently, their primary contributions arise from d_{xz} and d_{yz} orbitals, respectively. An intriguing observation is that the $d_{x^2-y^2}$ orbital, which aligns directly with the coupling directions of J_{2b} and J_{2c} , contributes the least. This suggests that the direct exchange is relatively small due to the greater distance associated with J_2 and stands in stark contrast to the large contribution of d_{xy} to J_1 . Taken together, it becomes evident that the indirect superexchange through the Sb layers adjacent to the Mn layer plays a significant role in determining the magnitude of J_2 . Conversely, J_{2b} exhibits a slightly larger value than J_{2c} , possibly attributable to the former's shorter bond length compared to the latter, resulting from the subtle structural distortion.

tion. The contributions from each d -orbital as functions of the Fermi level are shown in Fig. 4.

The interlayer exchange couplings are notably weaker owing to the substantial distance between Mn layers along the \mathbf{a} (\hat{z}) direction. The closest interlayer coupling J_a is identified as FM with a value of -0.029 meV, consistent with the experimental C-type spin ordering listed in Table II.

When compared to the experimental SJ values acquired through INS, presented in the last column of Table I, it becomes evident that the calculated SJ values are higher than the experimental values. Nonetheless, it is essential to highlight that the calculated trend in SJ values continues to align with the experimental trend. This underscores the consistency between the theoretical predictions and experimental observations. The exchange interactions are also calculated by mapping multiple magnetic configurations, as detailed in Appendix B, to a minimalistic J_1 - J_2 - J_a Heisenberg model. Our findings reveal $J_1^{\text{eff}} = 22.47$ meV, $J_2^{\text{eff}} = 5.25$ meV, and $J_a^{\text{eff}} = -0.61$ meV. Both J_1^{eff} and J_2^{eff} shows good agreement with INS result and our linear response calculation. The values of J_1^{eff} and J_a^{eff} are consistent with those reported in a prior DFT study [7], whereas J_a^{eff} is approximately one order of magnitude larger than both the INS results and our linear response calculations. Overall, as we demonstrate later, the values of J_1 , J_2 , and J_2/J_1 calculated using the linear response theory exhibit better agreement with experimental data when compared to the mapping method.

Figure 5 (a) illustrates the dependence of the exchange parameters J_1 and J_2 as functions of band filling within a rigid-band approximation. With hole doping, both J_1 and J_2 increase slightly before decreasing. The energy range spanning from -0.5 eV to E_F is primarily governed by Sb- $5p$ states in the density of states (DOS), with Mn- $3d$ states contributing minimally, as depicted in Figure 5 (b). As a result, the values of J_1 and J_2 exhibit only marginal alterations in the range of 0.1 – 0.45 hole/f.u. doping due to the dominant contribution of specific orbitals, namely d_{xy} and d_{xz} (or d_{yz}), which exhibit negligible DOS in this interval as depicted in Figure 6. The marginal changes indicate a slight increase in T_N with weak hole doping, in good agreement with previous findings [44].

With the introduction of electron doping, both J_1 and J_2 experience rapid amplitude reductions. Remarkably, J_2 undergoes a substantial alteration, transitioning to a weakly FM interaction. The ratio of J_1 and J_2 is illustrated in Figure 5 (c). In the doping range of 0.77 hole/f.u. to 0.11 electron/f.u., the magnetic system exhibits pronounced frustration. However, as the electron doping increases from 0.11 to 0.77 electron/f.u., the AFM order becomes stabilized. Beyond 0.77 electron/f.u. doping, the magnetic frustration resurfaces. The red dashed lines indicate the points where the square lattice reaches maximum frustration, residing on the boundary between checkerboard and stripe AFM configurations. Interest-

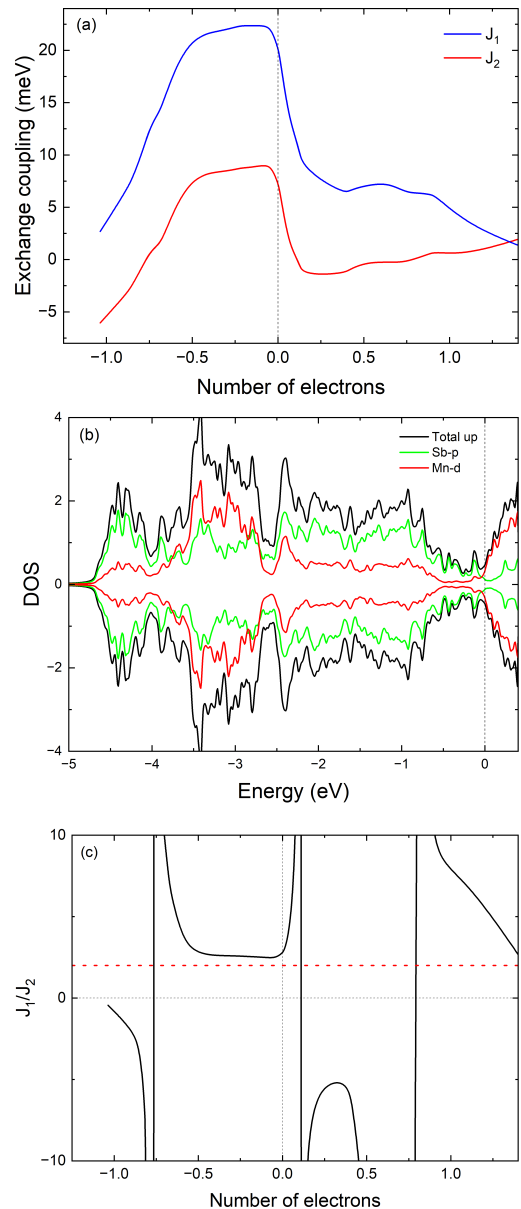


FIG. 5. DOS and exchange parameters J_1 and J_2 of one Mn site of SrMnSb_2 as functions of bandfilling in TB. Fermi level is shifted to zero. The panel (a) shows J_1 and J_2 as functions of bandfilling or electron and hole doping in units of electron(hole) per f.u. in TB. The panel (b) shows the total DOS, DOS for Sb p -states and DOS for Mn d -states, with units of number of states per formula unit per eV. The panel (c) shows the change of the ratio of J_1 and J_2 as a function of doping, where the horizontal dashed lines (red) is 2.

ingly, achieving this ratio through carrier doping seems challenging. In conclusion, the magnetic structure is expected to remain unchanged if the system is carrier doped, as predicted by the rigid-band calculation, which aligns with previous hole-doping investigations [44].

The behavior of J_1 and J_2 is closely aligned due to the gradual increase in the DOS of d_{xy} and d_{xz} (or d_{yz}), with

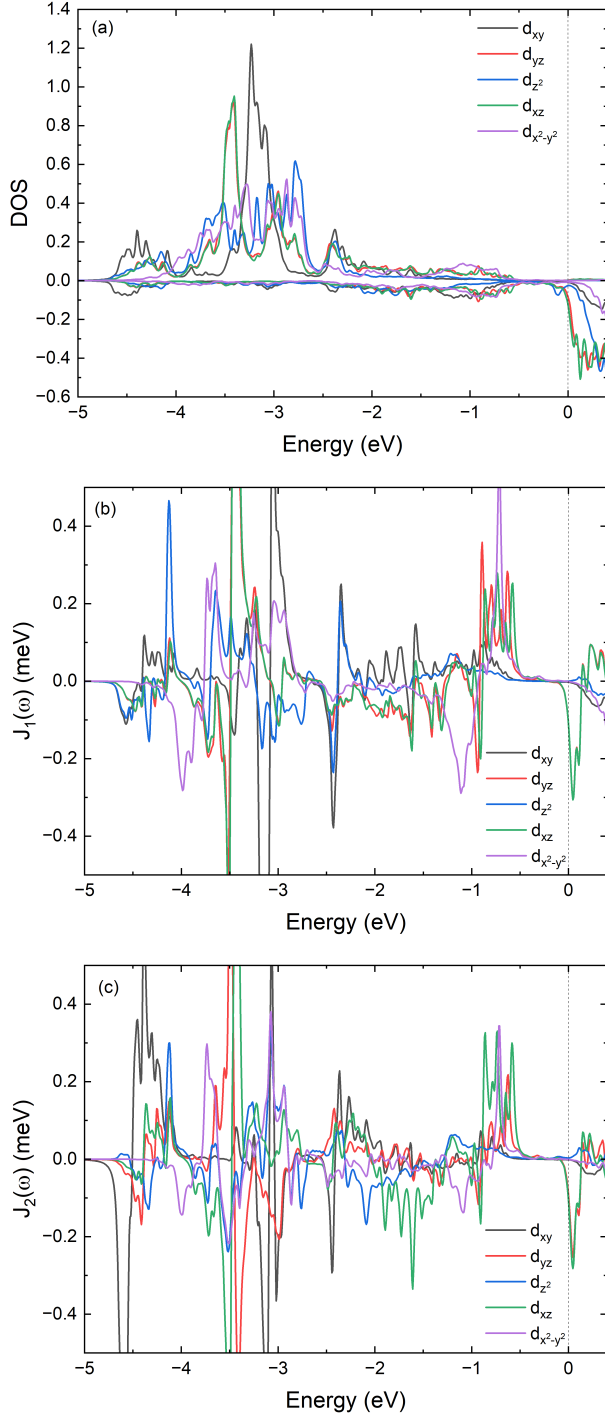


FIG. 6. The projected DOS for a single Mn site illustrated in Panel (a) and the orbital-resolved exchange coupling as a function of energy depicted in Panels (b) and (c).

J_1 in turn receiving contributions from nearly degenerate orbitals d_{xz} and d_{yz} , as depicted in Figure 6 (b) and (c). As the DOS of d_{xy} becomes dominant and subsequently begins to decline, while the DOS of d_{xz} (or d_{yz}) persists in its ascent, a pivotal shift occurs. Around the electron count of 1.35, J_1 and J_2 intersect, a consequence of the

declining DOS of d_{xy} contrasting with the oscillation of the DOS of d_{xz} (or d_{yz}). Overall, with five electrons in the 3d shell, the majority Mn-3d is nearly fully occupied while the minority channel is barely occupied, resulting in a large magnetic moment in the absence of doping. With the rigid-band picture, one would expect that electron or hole doping decreases the on-site magnetic Mn moment, by increasing (or decreasing) the electron occupancy in the minority (majority) spin channel, resulting in a smaller on-site Mn moment.

C. Spin wave spectra

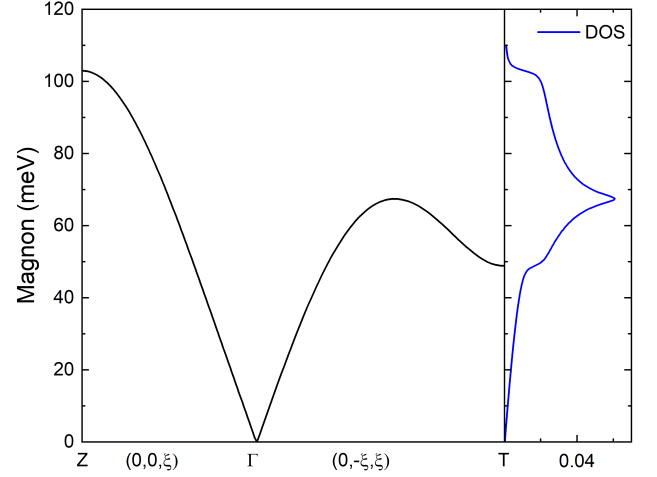


FIG. 7. Magnon band structure and DOS in SrMnSb2 calculated using J_1 and J_2 parameters obtained from DFT. Magnetocrystalline anisotropy is not included. High-symmetry k points Z and T are illustrated in Fig. 1.

Starting from the C-type ground state and dominant J_1 and J_2 values listed in Table I, we calculate the magnon dispersion using the LSWT. The calculated SW spectra along the Y- Γ -T path are displayed in Figure S1. It is important to note that Γ -Y $[(0, 0, \xi)]$ corresponds to the J_{2b} direction, while Γ -T $[(0, -\xi, \xi)]$ is slightly deviated from the J_1 direction. The calculation slightly overestimates the magnon bandwidth, but the dispersions are in overall good agreement with INS measurements described below. For a detailed comparison of the values of J_1 obtained using both symmetrized and unsymmetrized Hamiltonians, as well as spin wave spectra calculated along high-symmetry directions, please refer to Section I in the supplemental material [45].

Figure 8 shows the INS data (a-c) and simulations (d-f) of the spin wave spectra along three high-symmetry directions $(0, 1, L)$ (Γ -Y), $(0, 1/2 - K, 1/2 + K)$ (Γ -T), and $(H, 1, 0)$ (Γ -X). The simulations are done through experimentally determined parameters. Constant energy cuts of the data were taken and peaks in the cuts were fits to Gaussian functions in order to determine the peak

center for a given E . The extracted peak centers of the energy line cuts are presented in Fig. 9. The data treatment and modelling and the cuts and fits are given in Section II of the supplemental material [45].

To understand the INS data, we calculate the spin wave spectra using LSWT with two models. Model 1 enforces $J_{2b} = J_{2c}$, and model 2 keeps J_{2b} and J_{2c} as free parameters. The fitted single-ion anisotropy SD , in-plane magnetic interactions J_1 , J_{2b} , J_{2c} , and inter-layer interaction J_a are summarized in Table II. In model 1, the magnon bands are two-fold degenerate, whereas in model 2, the difference in J_{2b} and J_{2c} breaks the degeneracy and split the bands. Due to the small difference between J_{2b} and J_{2c} , and relatively coarse energy resolution used for our measurements, the splitting is not observed in the INS data. Nonetheless, it can be seen that model 2 gives a slightly better fit to the dispersion with a smaller reduced χ^2 ($r\chi^2$) compared to model 1, as shown in Fig. 9 and Table II.

In summary, our computed intralayer interactions (J_1 , J_{2b} , and J_{2c}) as well as the interlayer interaction (J_a) closely align with the observed values from INS. The spin wave dispersion derived from first-principle calculations, as depicted in Figure S1, exhibit an excellent agreement with those computed using experimental SJ values. Notably, the primary discrepancy lies in the bandwidth of the dispersion, a consequence of the overestimated SJ values originating from the ab initio calculations. Nonetheless, the concordance between the theoretical predictions and the experimentally-derived SJ -based calculations affirms the accuracy of our first-principle methodology in effectively predicting magnetic interactions within the materials.

TABLE II. Parameters and single-ion anisotropy (SD) and magnetic interactions from two models.

Model	SD	SJ_1	SJ_{2b}	SJ_{2c}	SJ_a	$r\chi^2$
1	-0.26(6)	27.51(6)	9.36(2)	9.36(2)	-0.092(6)	15.04
2	-0.2559(9)	27.96(1)	11.19(5)	7.78(9)	-0.091(3)	4.79

IV. CONCLUSIONS

This study on SrMnSb_2 presents a holistic understanding of its electronic and magnetic properties, achieved through a synergy of theoretical methodologies and experimental data. The exploration of exchange coupling parameters in SrMnSb_2 is carried out using linear response theory within a realistic TB model. Our calculated intralayer interactions (J_1 , J_{2b} , and J_{2c}) and inter-layer interaction (J_a) are in good agreement with INS results. Moreover, the study reveals a sizable AFM NNN exchange coupling J_2 , introducing significant spin frustration within the basal plane. Orbital-resolved contributions to exchange couplings help reveal the microscopic origin of the exchange interactions. Notably, we find that

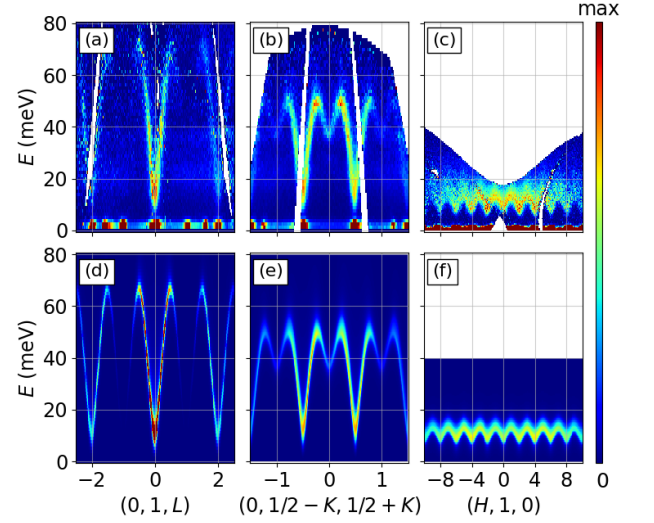


FIG. 8. INS data (a-c) and simulations by experimental parameters (d-f) of the spin wave spectra along three high-symmetry directions $(0, 1, L)$ (Γ -Y), $(0, 1/2 - K, 1/2 + K)$ (Γ -T), and $(H, 1, 0)$ (Γ -X).

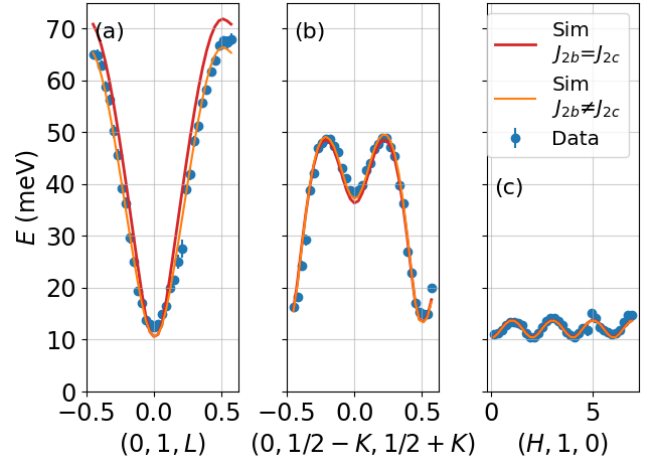


FIG. 9. Magnon dispersion along three high-symmetry directions determined from fits to the INS data. Lines show fits to the dispersion using the two different model Hamiltonians discussed in the text. Model 1 with $J_{2b} = J_{2c}$ is shown as red solid line while model 2 with $J_{2b} \neq J_{2c}$ is shown as orange solid line.

the NN exchange coupling J_1 in SrMnSb_2 predominantly arises from the contributions of Mn d_{xy} orbitals, aligning with the nearest Mn-Mn bond, while J_{2b} and J_{2c} receive primary contributions from d_{xz} and d_{yz} orbitals, respectively. This reflects the dominance of direct-exchange and superexchange nature for J_1 and J_2 , respectively. The band-filling dependence of exchange coupling based on the rigid-band model reveals that electron doping is expected to weaken both J_1 and J_2 while relieving spin

frustration through increasing the J_1/J_2 ratio. Moreover, the magnetic structure of SrMnSb₂ is anticipated to remain unaltered under carrier doping, which is in agreement with previous hole-doping investigations [44]. Applying an additional Hubbard-like U potential in DFT to Mn-3d orbitals promotes the localization of Mn-3d electrons and decreases the intersite exchange couplings overall and magnon bandwidth, resulting in better agreement with experiments. Future investigations can apply parameter-free beyond-DFT approaches [14] to further improve the description of magnetic interactions and excitations in SrMnSb₂. In summary, this investigation not only advances our comprehension of SrMnSb₂ but also underscores the efficacy of combining ab initio and experimental methods in elucidating intricate materials and their magnetic interactions.

V. ACKNOWLEDGMENTS

This work is supported by the U.S. Department of Energy, Office of Basic Energy Sciences, Division of Materials Sciences and Engineering. Ames Laboratory is operated for the U.S. Department of Energy by Iowa State University under Contract No. DE-AC02-07CH11358. This research used resources at the Spallation Neutron Source, a DOE Office of Science User Facility operated by the Oak Ridge National Laboratory.

Appendix A: Hamiltonian Symmetrization

Wannier functions (WF) are localized atomic-like orbitals defined at each atom site. For a set of isolated bands that are separated from all other lower and higher bands throughout the BZ by band gaps, its electronic states can be well described by a set of WFs $|w_{\vec{R}}^{\mu}\rangle$ where \vec{R} is the location of the unit cell considered and μ the index of WFs in the cell. For a multiple-site system, μ is a combination of quantum numbers n_i, l_i, m_i, σ_i and site position vectors τ_i with index i for sites that can only be $(0, 0, 0)$ for single-site system.

When a WF is rotated by one point symmetry $\hat{\mathcal{R}}$ of the system, it can only vary between WFs belong to equivalent sites with the same quantum numbers n_i and l_i , that is, the symmetry can only mix states with different magnetic quantum numbers and spins

$$\hat{\mathcal{R}}|w_{\vec{R}+\vec{\tau}_i}^{\beta_i m_i \sigma_i}\rangle = \sum_{m'_i \sigma'_i} \mathcal{R}_{m'_i \sigma'_i m_i \sigma_i}^{l_i} |w_{\vec{R}'+\vec{\tau}'_i}^{\beta_i m'_i \sigma'_i}\rangle. \quad (\text{A1})$$

where $\hat{\mathcal{R}}(\vec{R} + \vec{\tau}_i) = \vec{R}' + \vec{\tau}'_i$ and β_i the combination of n_i and l_i . According to the orthogonalization of WFs, the transform matrix elements $\langle w_{\vec{R}'+\vec{\tau}'_i}^{\beta_i m'_i \sigma'_i} | \hat{\mathcal{R}} | w_{\vec{R}+\vec{\tau}_i}^{\beta_i m_i \sigma_i} \rangle$ are given by

$$\mathcal{R}_{m'_i \sigma'_i m_i \sigma_i}^{l_i} = S_{m'_i \sigma'_i, m_i \sigma_i}^{l_i} \delta_{\vec{R}'+\vec{\tau}'_i, \hat{\mathcal{R}}(\vec{R}+\vec{\tau}_i)} \delta_{\beta_i, \beta'_i}, \quad (\text{A2})$$

It is obvious that the transform matrix \mathcal{R} should be l and site diagonal.

The transform matrix \mathcal{R} can be obtained by the behavior of WANNIER90's basis orbitals under symmetry operations. Wannier90 uses real spherical harmonics $\mathcal{Y}_{l,m}$ which is related to complex spherical harmonics Y_l^m by

$$\begin{aligned} \mathcal{Y}_{l,m} &= \begin{cases} \sqrt{2}(-1)^m \Re\{Y_l^{|m|}(\theta, \phi)\} & m > 0 \\ \sqrt{2}(-1)^m \Im\{Y_l^{-|m|}(\theta, \phi)\} & m < 0 \\ \Re\{Y_{lm}(\theta, \phi)\} & m = 0 \end{cases} \\ &= \begin{cases} \frac{1}{\sqrt{2}} [Y_l^{-|m|} + (-1)^m Y_l^{|m|}] & m > 0 \\ \frac{i}{\sqrt{2}} [Y_l^{-|m|} - (-1)^m Y_l^{|m|}] & m < 0 \\ Y_l^0 & m = 0 \end{cases}. \quad (\text{A3}) \end{aligned}$$

This equation defines the unitary transform matrix $\mathbf{U}_{\mathbb{C} \rightarrow \mathbb{R}}$ between $\mathcal{Y}_{l,m}$ and Y_l^m . The angular momentum operator \hat{L} in the basis of real spherical harmonics can then be written as

$$\hat{L}^{\mathbb{R}} = \mathbf{U}_{\mathbb{C} \rightarrow \mathbb{R}} \hat{L}^{\mathbb{C}} \mathbf{U}_{\mathbb{C} \rightarrow \mathbb{R}}^\dagger = \mathbf{U}_{\mathbb{C} \rightarrow \mathbb{R}} \hat{L}^{\mathbb{C}} \mathbf{U}_{\mathbb{R} \rightarrow \mathbb{C}}. \quad (\text{A4})$$

In the presentation of complex spherical harmonics Y_ℓ^m , the non-vanished matrix elements of $\hat{L}^{\mathbb{C}}$ are

$$\begin{aligned} \langle l, m | \hat{L}_z | l, m \rangle &= \hbar m, \\ \langle l, m-1 | \hat{L}_- | l, m \rangle &= \hbar \sqrt{l(l+1) - m(m-1)}, \\ \langle l, m+1 | \hat{L}_+ | l, m \rangle &= \hbar \sqrt{l(l+1) - m(m+1)}. \end{aligned} \quad (\text{A5})$$

One can construct in the representation of real spherical harmonics rotations given by

$$\hat{\mathcal{R}}^Y = e^{-i\hat{\mathbf{n}} \cdot \hat{L}^{\mathbb{C}} \phi}, \quad (\text{A6})$$

where $\hat{\mathbf{n}}$ is the axis of the rotation symmetry and ϕ the rotation angle. Then the transform matrix \mathcal{R} can be obtained by

$$\hat{\mathcal{R}}^Y = \mathbf{U}_{\mathbb{C} \rightarrow \mathbb{R}} \hat{\mathcal{R}}^Y \mathbf{U}_{\mathbb{R} \rightarrow \mathbb{C}} = \mathbf{U}_{\mathbb{C} \rightarrow \mathbb{R}} e^{-i\hat{\mathbf{n}} \cdot \hat{L}^{\mathbb{C}} \phi} \mathbf{U}_{\mathbb{R} \rightarrow \mathbb{C}}. \quad (\text{A7})$$

The rotation on spinor can be written as

$$\hat{\mathcal{R}}^{\hat{\sigma}} = e^{-i\hat{\mathbf{n}} \cdot \hat{S} \phi}. \quad (\text{A8})$$

The spin angular momentum operator \hat{S} is defined as

$$\hat{S} = \frac{\hbar}{2} (\sigma_x, \sigma_y, \sigma_z), \quad (\text{A9})$$

where σ_x, σ_y and σ_z are Pauli matrices given by

$$\sigma_x = \begin{pmatrix} 0 & 1 \\ 1 & 0 \end{pmatrix}, \quad \sigma_y = \begin{pmatrix} 0 & -i \\ i & 0 \end{pmatrix}, \quad \sigma_z = \begin{pmatrix} 1 & 0 \\ 0 & -1 \end{pmatrix} \quad (\text{A10})$$

Thus, in the representation of real spherical harmonics and spinor, the rotation is given by $\mathcal{R} = \hat{\mathcal{R}}^Y \hat{\mathcal{R}}^{\hat{\sigma}}$.

The Hamiltonian \hat{H} of a system is invariant under its all symmetry operations

$$\hat{H} = \hat{\mathcal{R}} \hat{H} \hat{\mathcal{R}}^\dagger. \quad (\text{A11})$$

The elements of real-space Hamiltonian are defined by $H_{ij}^{\vec{R}} = \langle w_{\tau_i}^{\beta_i m_i \sigma_i} | \hat{H} | w_{\vec{R}+\tau_j}^{\beta_j m_j \sigma_j} \rangle$ that under symmetry operations transforms as

$$\begin{aligned}
H_{ij}^{\vec{R}} &= \langle w_{\tau_i}^{\beta_i m_i \sigma_i} | \hat{H} | w_{\vec{R}+\tau_j}^{\beta_j m_j \sigma_j} \rangle \\
&= \langle w_{\tau_i}^{\beta_i m_i \sigma_i} | \hat{\mathcal{R}} \hat{H} \hat{\mathcal{R}}^\dagger | w_{\vec{R}+\tau_j}^{\beta_j m_j \sigma_j} \rangle \\
&= \sum_{\mu\mu', \vec{R}'_i, \vec{R}'_j} \langle w_{\tau_i}^{\beta_i m_i \sigma_i} | \hat{\mathcal{R}} | w_{\vec{R}'_i+\tau'_i}^{\beta'_i m'_i \sigma'_i} \rangle \langle w_{\vec{R}'_i+\tau'_i}^{\beta'_i m'_i \sigma'_i} | \hat{H} | w_{\vec{R}'_j+\tau'_j}^{\beta'_j m'_j \sigma'_j} \rangle \\
&\times \langle w_{\vec{R}'_j+\tau'_j}^{\beta'_j m'_j \sigma'_j} | \hat{\mathcal{R}}^\dagger | w_{\vec{R}+\tau_j}^{\beta_j m_j \sigma_j} \rangle \\
&= \sum_{m'_i \sigma'_i m'_j \sigma'_j} \mathcal{R}_{m_i \sigma_i, m'_i \sigma'_i}^{\beta_i} \delta_{\vec{\tau}_i, \hat{S}(\vec{R}'_i+\vec{\tau}'_i)} \delta_{n_i, n'_i} \delta_{l_i, l'_i} \\
&\times \langle w_{\vec{R}'_i+\tau'_i}^{\beta'_i m'_i \sigma'_i} | \hat{H} | w_{\vec{R}'_j+\tau'_j}^{\beta'_j m'_j \sigma'_j} \rangle \\
&\times \mathcal{R}_{m'_j \sigma'_j, m_j \sigma_j}^{l_j*} \delta_{\hat{\mathcal{R}}(\vec{R}'_j+\vec{\tau}'_j), \vec{R}+\vec{\tau}_j} \delta_{n_j, n'_j} \delta_{l_j, l'_j} \\
&= \sum_{m'_i \sigma'_i m'_j \sigma'_j} \mathcal{R}_{m_i \sigma_i, m'_i \sigma'_i}^{\beta_i} \delta_{\vec{\tau}_i, \hat{\mathcal{R}}(\vec{R}'_i+\vec{\tau}'_i)} \delta_{n_i, n'_i} \delta_{l_i, l'_i} H_{ij}^{\vec{R}'_j-\vec{R}'_i} \\
&\times \mathcal{R}_{m'_j \sigma'_j, m_j \sigma_j}^{l_j*} \delta_{\hat{\mathcal{R}}(\vec{R}'_j+\vec{\tau}'_j), \vec{R}+\vec{\tau}_j} \delta_{n_j, n'_j} \delta_{l_j, l'_j}. \quad (\text{A12})
\end{aligned}$$

If a Hamiltonian does not satisfy the system's symmetry, its symmetrized Hamiltonian can be obtained as the average over all symmetry operations given by

$$H^{\text{sym}} = \frac{1}{|\mathcal{G}_H|} \sum_{\mathcal{R} \in \mathcal{G}_H} \mathcal{R} H \mathcal{R}^\dagger. \quad (\text{A13})$$

where $|\mathcal{G}_H|$ is the number of symmetry operators in the

group \mathcal{G}_H .

Appendix B: Calculate J_{ij} by mapping Total energy calculations

For SrMnSb_2 , one can construct a supercell with basis vectors \mathbf{a} , $\mathbf{b}+\mathbf{c}$ and $\mathbf{b}-\mathbf{c}$ and simulate four magnetic configurations, C-AFM, A-AFM, G-AFM and S-AFM using *ab initio* package. Fit the Heisenberg energy to the calculated total energy.

$$\begin{aligned}
4E_A/S^2 &= 2J_1+2J_2 - J_c/2, \\
4E_G/S^2 &= -2J_1+2J_2 - J_c/2, \\
4E_{\text{SA}}/S^2 &= -2J_2 - J_c/2, \\
4E_C/S^2 &= -2J_1+2J_2 + J_c/2, \quad (\text{B1})
\end{aligned}$$

where the energies E_A , E_G , E_{SA} and E_C are the calculated total energy per magnetic atom for the four configurations. Here we do not distinguish J_{2b} and J_{2c} , instead, an average of them as J_2 is calculated. Then the exchange coupling constants are given by

$$\begin{aligned}
J_c &= 4(E_C - E_G)/S^2, \\
J_1 &= (E_A - E_G)/S^2, \\
J_2 &= (E_A - E_{\text{SA}})/S^2 - J_1/2. \quad (\text{B2})
\end{aligned}$$

-
- [1] J. M. Wilde, S. X. M. Riberolles, A. Das, Y. Liu, T. W. Heitmann, X. Wang, W. E. Straszheim, S. L. Bud'ko, P. C. Canfield, A. Kreyssig, R. J. McQueeney, D. H. Ryan, and B. G. Ueland, Canted antiferromagnetic phases in the candidate layered weyl material EuMnSb_2 , *Phys. Rev. B* **106**, 024420 (2022).
- [2] M. Z. Hasan and C. L. Kane, Colloquium: Topological insulators, *Rev. Mod. Phys.* **82**, 3045 (2010).
- [3] A. Bansil, H. Lin, and T. Das, Colloquium: Topological band theory, *Rev. Mod. Phys.* **88**, 021004 (2016).
- [4] N. P. Armitage, E. J. Mele, and A. Vishwanath, Weyl and dirac semimetals in three-dimensional solids, *Rev. Mod. Phys.* **90**, 015001 (2018).
- [5] B. Q. Lv, T. Qian, and H. Ding, Experimental perspective on three-dimensional topological semimetals, *Rev. Mod. Phys.* **93**, 025002 (2021).
- [6] D. Vanderbilt, *Berry Phases in Electronic Structure Theory: Electric Polarization, Orbital Magnetization and Topological Insulators* (Cambridge University Press, Cambridge, England, 2018).
- [7] Q. Zhang, S. Okamoto, M. B. Stone, J. Liu, Y. Zhu, J. DiTusa, Z. Mao, and D. A. Tennant, Influence of magnetism on dirac semimetallic behavior in nonstoichiometric $\text{Sr}_{1-y}\text{Mn}_{1-z}\text{Sb}_2$ ($y \sim 0.07, z \sim 0.02$), *Phys. Rev. B* **100**, 205105 (2019).
- [8] H. A. Ceccatto, C. J. Gazza, and A. E. Trumper, J_1 - J_2 model: Energy, correlations, and order-parameter fluctuations on finite lattices, *Phys. Rev. B* **45**, 7832 (1992).
- [9] J. Sirker, Z. Weihong, O. P. Sushkov, and J. Oitmaa, J_1 - J_2 model: First-order phase transition versus deconfinement of spinons, *Physical Review B* **73**, 184420 (2006).
- [10] A. Liechtenstein, M. Katsnelson, V. Antropov, and V. Gubanov, Local spin density functional approach to the theory of exchange interactions in ferromagnetic metals and alloys, *Journal of Magnetism and Magnetic Materials* **67**, 65 (1987).
- [11] T. Kotani and M. van Schilfgaarde, Spin wave dispersion based on the quasiparticle self-consistent gw method: NiO , MnO and $\alpha\text{-MnAs}$, *Journal of Physics: Condensed Matter* **20**, 295214 (2008).
- [12] M. van Schilfgaarde, T. Kotani, and S. Faleev, Quasiparticle self-consistent GW theory, *Phys. Rev. Lett.* **96**, 226402 (2006).
- [13] L. Ke, M. van Schilfgaarde, J. Pulikkotil, T. Kotani, and V. Antropov, Low-energy coherent stoner-like excitations in CaFe_2As_2 , *Phys. Rev. B: Rapid communication* **83**, 060404 (2011).

- [14] L. Ke and M. I. Katsnelson, Electron correlation effects on exchange interactions and spin excitations in 2D van der Waals materials, *npj Computational Materials* **7**, 1 (2021).
- [15] N. Marzari and D. Vanderbilt, Maximally localized generalized wannier functions for composite energy bands, *Physical Review B* **56**, 12847 (1997).
- [16] I. Souza, N. Marzari, and D. Vanderbilt, Maximally localized wannier functions for entangled energy bands, *Phys. Rev. B* **65**, 035109 (2001).
- [17] N. Marzari, A. A. Mostofi, J. R. Yates, I. Souza, and D. Vanderbilt, Maximally localized wannier functions: Theory and applications, *Rev. Mod. Phys.* **84**, 1419 (2012).
- [18] L. Ke, Intersublattice magnetocrystalline anisotropy using a realistic tight-binding method based on maximally localized Wannier functions, *Phys. Rev. B* **99**, 054418 (2019).
- [19] E. Brechtel, G. Cordier, and H. Schäfer, Neue ternäre erdalkali-übergangselement-pnictide, *Journal of the Less Common Metals* **79**, 131 (1981).
- [20] B. Li, D. M. Pajerowski, S. X. M. Riberolles, L. Ke, J.-Q. Yan, and R. J. McQueeney, Quasi-two-dimensional ferromagnetism and anisotropic interlayer couplings in the magnetic topological insulator mnbi_2te_4 , *Phys. Rev. B* **104**, L220402 (2021).
- [21] V. V. Mkhitarian and L. Ke, Self-consistently renormalized spin-wave theory of layered ferromagnets on the honeycomb lattice, *Phys. Rev. B* **104**, 064435 (2021).
- [22] J. P. Perdew, K. Burke, and M. Ernzerhof, Generalized gradient approximation made simple, *Phys. Rev. Lett.* **77**, 3865 (1996).
- [23] G. Kresse and D. Joubert, From ultrasoft pseudopotentials to the projector augmented-wave method, *Phys. Rev. B* **59**, 1758 (1999).
- [24] G. Kresse and J. Furthmüller, Efficient iterative schemes for ab initio total-energy calculations using a plane-wave basis set, *Phys. Rev. B* **54**, 11169 (1996).
- [25] A. A. Mostofi, J. R. Yates, G. Pizzi, Y.-S. Lee, I. Souza, D. Vanderbilt, and N. Marzari, An updated version of wannier90: A tool for obtaining maximally-localised wannier functions, *Computer Physics Communications* **185**, 2309 (2014).
- [26] M. van Schilfgaarde and V. P. Antropov, First-principles exchange interactions in Fe, Ni, and Co, *Journal of Applied Physics* **85**, 4827 (1999).
- [27] L. Ke and V. van Schilfgaarde, Mark aand Antropov, Spin excitations in $\text{K}_2\text{Fe}_{4+x}\text{Se}_5$: Linear response approach, *Phys. Rev. B: Rapid communication* **86**, 020402 (2012).
- [28] L. Ke, B. N. Harmon, and M. J. Kramer, Electronic structure and magnetic properties in $T_2\text{AlB}_2$ ($T=\text{Fe, Mn, Cr, Co, and Ni}$) and their alloys, *Phys. Rev. B* **95**, 104427 (2017).
- [29] L. Ke and D. D. Johnson, Intrinsic magnetic properties in $R(\text{Fe}_{1-x}\text{Co}_x)_{11}\text{TiZ}$ ($R=\text{Y and Ce; Z=H, C, and N}$), *Phys. Rev. B* **94**, 024423 (2016).
- [30] L. Ke, K. D. Belashchenko, M. van Schilfgaarde, T. Kotani, and V. P. Antropov, Effects of alloying and strain on the magnetic properties of Fe_{16}N_2 , *Phys. Rev. B* **88**, 024404 (2013).
- [31] G. Pizzi, V. Vitale, R. Arita, S. Blügel, F. Freimuth, G. Géranton, M. Gibertini, D. Gresch, C. Johnson, T. Koretsune, J. Ibañez-Azpiroz, H. Lee, J.-M. Lihm, D. Marchand, A. Marrazzo, Y. Mokrousov, J. I. Mustafa, Y. Nohara, Y. Nomura, L. Paulatto, S. Poncé, T. Ponweiser, J. Qiao, F. Thöle, S. S. Tsirkin, M. Wierzbowska, N. Marzari, D. Vanderbilt, I. Souza, A. A. Mostofi, and J. R. Yates, Wannier90 as a community code: new features and applications, *Journal of Physics: Condensed Matter* **32**, 165902 (2020).
- [32] D. M. Korotin, V. V. Mazurenko, V. I. Anisimov, and S. V. Streltsov, Calculation of exchange constants of the Heisenberg model in plane-wave-based methods using the Green's function approach, *Phys. Rev. B* **91**, 224405 (2015).
- [33] M. Blanco-Rey, J. I. Cerdá, and A. Arnau, Validity of perturbative methods to treat the spin-orbit interaction: application to magnetocrystalline anisotropy, *New Journal of Physics* **21**, 073054 (2019).
- [34] E. Rosenberg, J. M. DeStefano, Y. Guo, J. S. Oh, M. Hashimoto, D. Lu, R. J. Birgeneau, Y. Lee, L. Ke, M. Yi, and J.-H. Chu, Uniaxial ferromagnetism in the kagome metal TbV_6Sn_6 , *Phys. Rev. B* **106**, 115139 (2022), (*Editors' Suggestion*).
- [35] Y. Lee, R. Skomski, X. Wang, P. P. Orth, Y. Ren, B. Kang, A. K. Pathak, A. Kutepov, B. N. Harmon, R. J. McQueeney, I. I. Mazin, and L. Ke, Interplay between magnetism and band topology in the kagome magnets RMn_6Sn_6 , *Phys. Rev. B* **108**, 045132 (2023).
- [36] E. I. Timmons, S. Teknowijoyo, M. Kończykowski, O. Cavani, M. A. Tanatar, S. Ghimire, K. Cho, Y. Lee, L. Ke, N. H. Jo, S. L. Bud'ko, P. C. Canfield, P. P. Orth, M. S. Scheurer, and R. Prozorov, Electron irradiation effects on superconductivity in PdTe_2 : An application of a generalized Anderson theorem, *Phys. Rev. Research* **2**, 023140 (2020).
- [37] T. Holstein and H. Primakoff, Field dependence of the intrinsic domain magnetization of a ferromagnet, *Phys. Rev.* **58**, 1098 (1940).
- [38] S. Toth and B. Lake, Linear spin wave theory for single-q incommensurate magnetic structures, *Journal of Physics: Condensed Matter* **27**, 166002 (2015).
- [39] D. L. Abernathy, M. B. Stone, M. J. Loguillo, M. S. Lucas, O. Delaire, X. Tang, J. Y. Y. Lin, and B. Fultz, Design and operation of the wide angular-range chopper spectrometer ARCS at the Spallation Neutron Source, *Review of Scientific Instruments* **83**, 10.1063/1.3680104 (2012), 015114.
- [40] B. Li, bingli621/pylisw: pylisw v1.0 (2023).
- [41] J. Y. Liu, J. Hu, Q. Zhang, D. Graf, H. B. Cao, S. M. A. Radmanesh, D. J. Adams, Y. L. Zhu, G. F. Cheng, X. Liu, W. A. Phelan, J. Wei, M. Jaime, F. Balakirev, D. A. Tennant, J. F. DiTusa, I. Chiorescu, L. Spinu, and Z. Q. Mao, A magnetic topological semimetal $\text{Sr}_{1-y}\text{Mn}_{1-z}\text{Sb}_2$ ($y, z < 0.1$), *Nature Materials* **16**, 905 (2017).
- [42] Y. Liu, T. Ma, L. Zhou, W. E. Straszheim, F. Islam, B. A. Jensen, W. Tian, T. Heitmann, R. A. Rosenberg, J. M. Wilde, B. Li, A. Kreyssig, A. I. Goldman, B. G. Ueland, R. J. McQueeney, and D. Vaknin, Crystal growth, microstructure, and physical properties of SrMnSb_2 , *Physical Review B* **99**, 054435 (2019).
- [43] F. Islam, R. Choudhary, Y. Liu, B. G. Ueland, D. Paudyal, T. Heitmann, R. J. McQueeney, and D. Vaknin, Controlling magnetic order, magnetic anisotropy, and band topology in the semimetals $\text{Sr}(\text{Mn}_{0.9}\text{Cu}_{0.1})\text{Sb}_2$ and $\text{Sr}(\text{Mn}_{0.9}\text{Zn}_{0.1})\text{Sb}_2$,

- Phys. Rev. B **102**, 085130 (2020).
- [44] Y. Liu, F. Islam, K. W. Dennis, W. Tian, B. G. Ueland, R. J. McQueeney, and D. Vaknin, Hole doping and anti-ferromagnetic correlations above the Néel temperature of the topological semimetal $(\text{Sr}_{1-x}\text{K}_x)\text{MnSb}_2$, Phys. Rev. B **100**, 014437 (2019).
- [45] See Supplemental Material [url] for symmetrized exchange interactions, theoretical calculation of spin spectra and INS data treatment and modeling.

Magnetic interactions and excitations in SrMnSb₂

Supplemental Materials

Zhenhua Ning,⁴ Bing Li,⁴ Arnab Banerjee,⁵ Victor Fanelli,⁶ Doug Abernathy,⁶
Yong Liu,⁴ Benjamin G Ueland,⁴ Robert J. McQueeney,⁴ and Liqin Ke⁴

⁴*Ames National Laboratory, U.S. Department of Energy, Ames, Iowa 50011*

⁵*Department of Physics and Astronomy, Purdue University, West Lafayette, IN 47906*

⁶*Neutron Scattering Division, Oak Ridge National Laboratory, Oak Ridge, TN, 37831*

I. CALCULATED SPIN WAVE SPECTRA AND SYMMETRIZED J_1

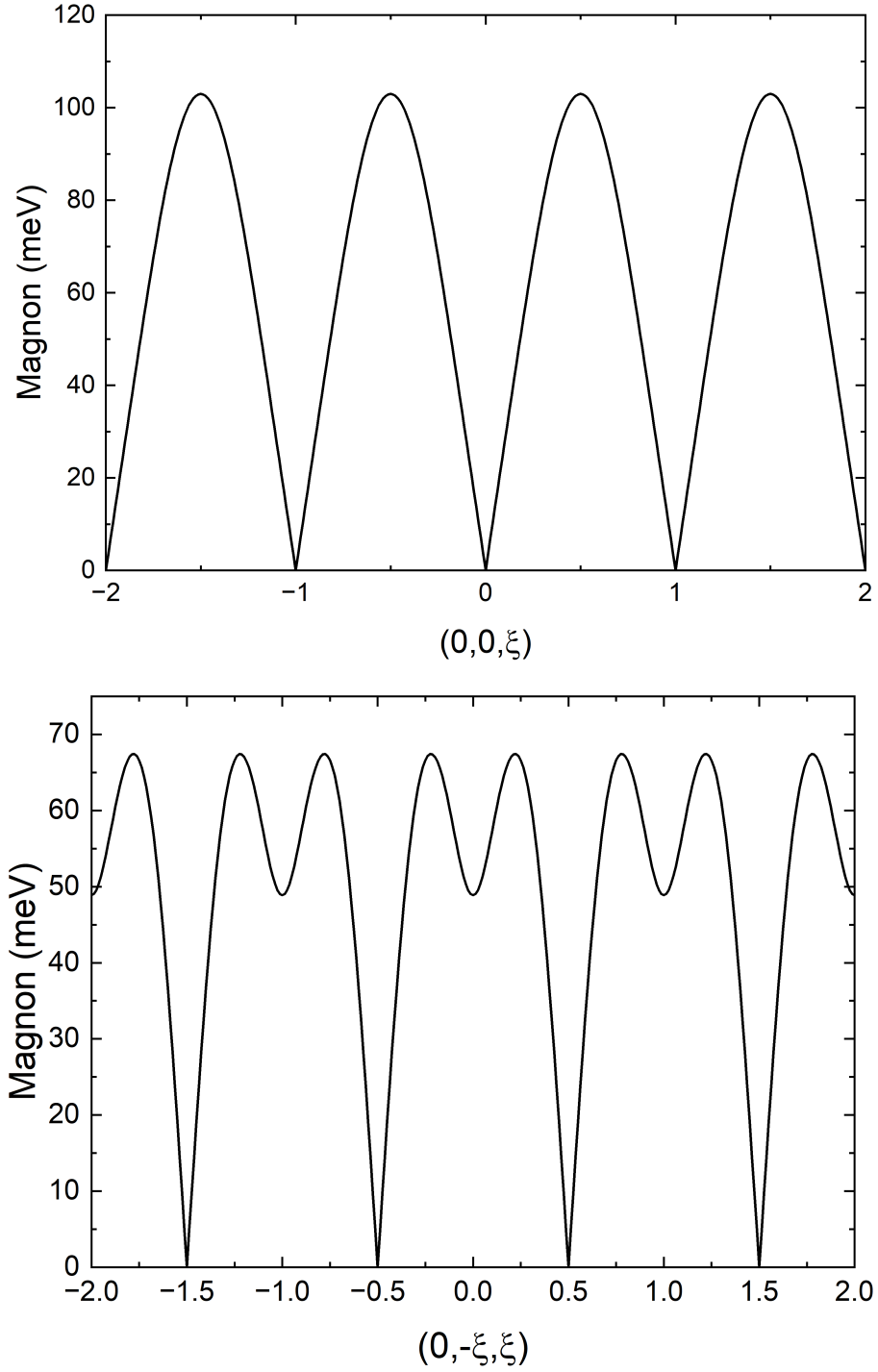


FIG. S1. Spinwave spectra of SrMnSb₂. Top panel is the spin wave dispersion along $(0,0,\xi)$ and bottom panel along $(0,-\xi,\xi)$.

With exchange parameters obtained by linear response theory, the spectra of spin wave is calculated using $J_1 - J_2 - J_a$ model given by

$$H = \sum_{\langle i,j \rangle}^{NN} J_1 \hat{\mathbf{S}}_i \cdot \hat{\mathbf{S}}_j + \sum_{\langle i,j \rangle}^{NNN} J_2 \hat{\mathbf{S}}_i \cdot \hat{\mathbf{S}}_j + \sum_{\langle i,j \rangle} J_a \mathbf{S}_i \cdot \mathbf{S}_j + \sum_i D(S_z)^2, \quad (\text{S1})$$

TABLE I. Real-space pairwise exchange parameters J_{ij} of SrMnSb₂ for the Heisenberg Hamiltonian for the star of neighbors, marked by primitive translation vectors \mathbf{R} . The first row is calculated with the symmetrized Hamiltonian while the second one is done with the non-symmetrized Hamiltonian. To show symmetry clearly, numbers assume up to the fifth decimal place.

\mathbf{R}	[0,0,0]	[0,-1,0]	[0,0,-1]	[0,-1,-1]
J_1^{sym} (meV)	11.23149	11.23149	11.23149	11.23149
J_1 (meV)	11.34235	11.32793	11.33891	11.34101

Table I presents the intra-sublattice interactions J_1 between nearest neighbors (NN) with a bond length of 3.14 Å. It is evident that the exchange parameters calculated using the symmetrized Hamiltonian are identical for the star of neighbors, whereas those obtained using the non-symmetrized Hamiltonian differ at the second decimal place. Despite the lack of symmetry, both sets of values agree within 0.6%. The intra-sublattice interactions between the next-nearest neighbors (NNN) exhibit similar symmetric behavior, with an average value of 7.12 meV. This value is less than half of J_1 , indicating frustration in NNN interactions.

II. DETAILS OF INS DATA TREATMENT AND MODELING

We focus on the three high-symmetry directions $(1, 0, L)$, $(0, 0.5 - K, 0.5 + K)$ and $(H, 1, 0)$, and plotted the spectra as functions of energy transfer E as shown in Figs. S2, S3, and S4, respectively. The bin ranges are shown in the title of each plot. The line cuts were fit to a Gaussian, shown by the blue curves, to extract the peak centers as shown in Fig.9 in the main text. In Figs. S2 and S3, a \mathbf{Q} -independent linear background was also introduced to account for the weak phonon signals from the aluminum sample holder.

To model the spin wave data, we chose the chemical unit cell with 4 Mn ions, and introduced in-plane interactions J_1 , J_2 , inter-layer interaction J_a , and an uniaxial single-ion anisotropy D . The magnetic Hamiltonian is given by Eq. (S1).

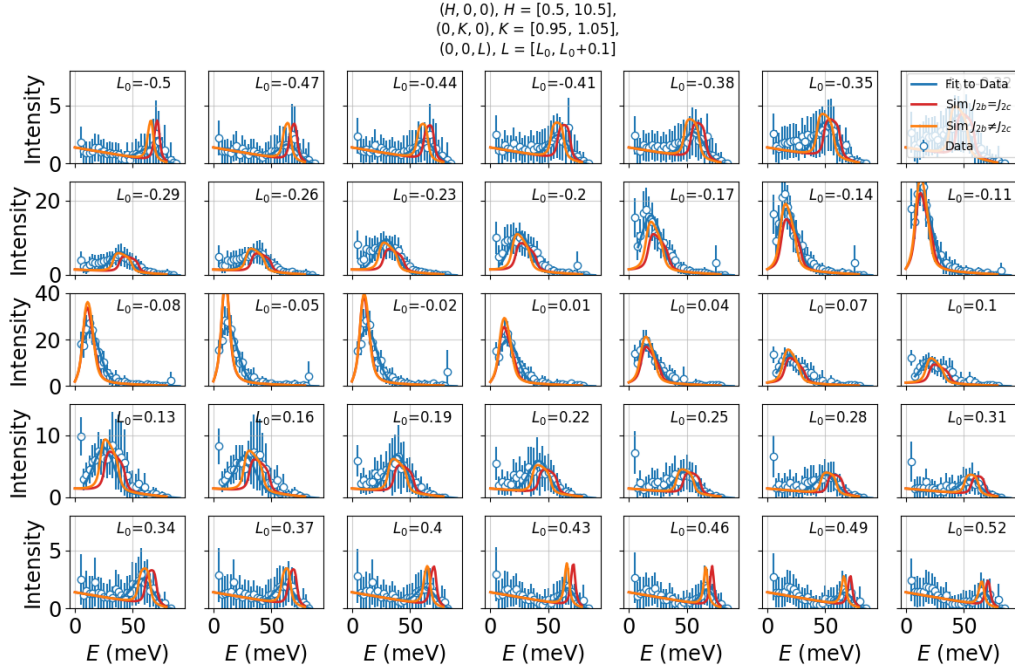


FIG. S2. Cuts of inelastic neutron scattering along $(0,1,L)$ made using the integration ranges indicated. Lines show fits using Gaussian functions and simulations using the two model Hamiltonians discussed in the text.

We implemented the linear spin wave theory to calculate the spin wave dispersion and INS spectra. We used the peak shape of the under-damped harmonic oscillator to model the INS spectra at each \mathbf{Q} point, where the damping parameters are chosen to be FWHM of the energy-dependent instrumental resolution of ARCS. We perform the same \mathbf{Q} -binning as in the data, and fit the energy line cuts to Gaussians to extract the peak centers. We then perform a

second round of fitting to find the magnetic interactions that best match the extracted peaks centers in the data and the model.

Figs. S2, S3, and S4 show the data compared to two models. Red curves were calculated from the fitting of peak centers while enforcing $J_{2b} = J_{2c}$, orange curves are from the fitting that keeps J_{2b} and J_{2c} as free parameters.

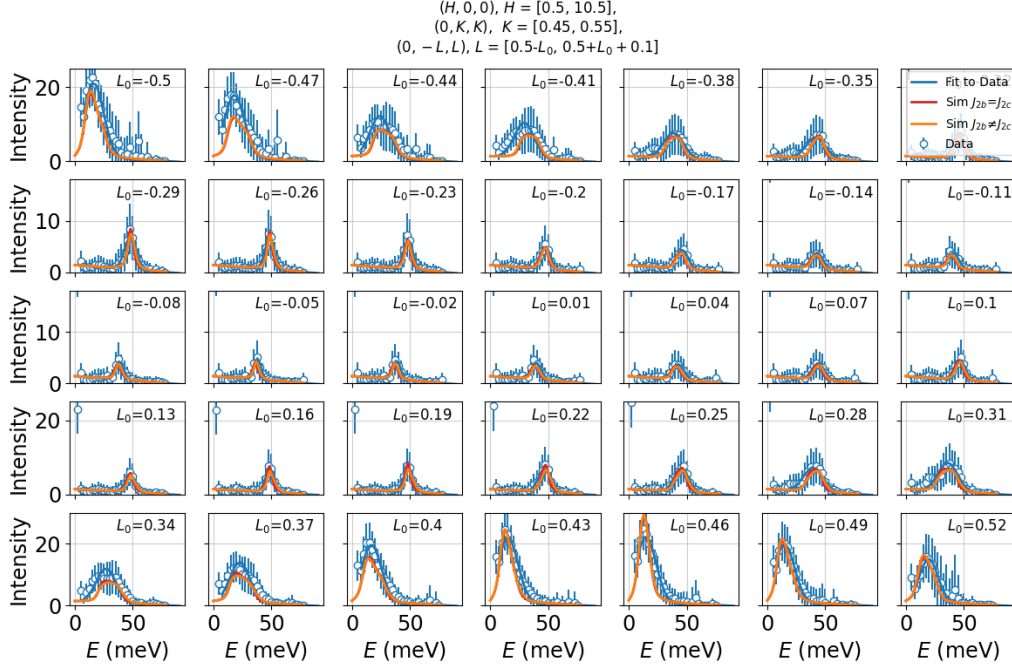


FIG. S3. Cuts of inelastic neutron scattering along $(0,1/2-K,1/2+K)$ made using the integration ranges indicated. Lines show fits using Gaussian functions and simulations using the two model Hamiltonians discussed in the text.

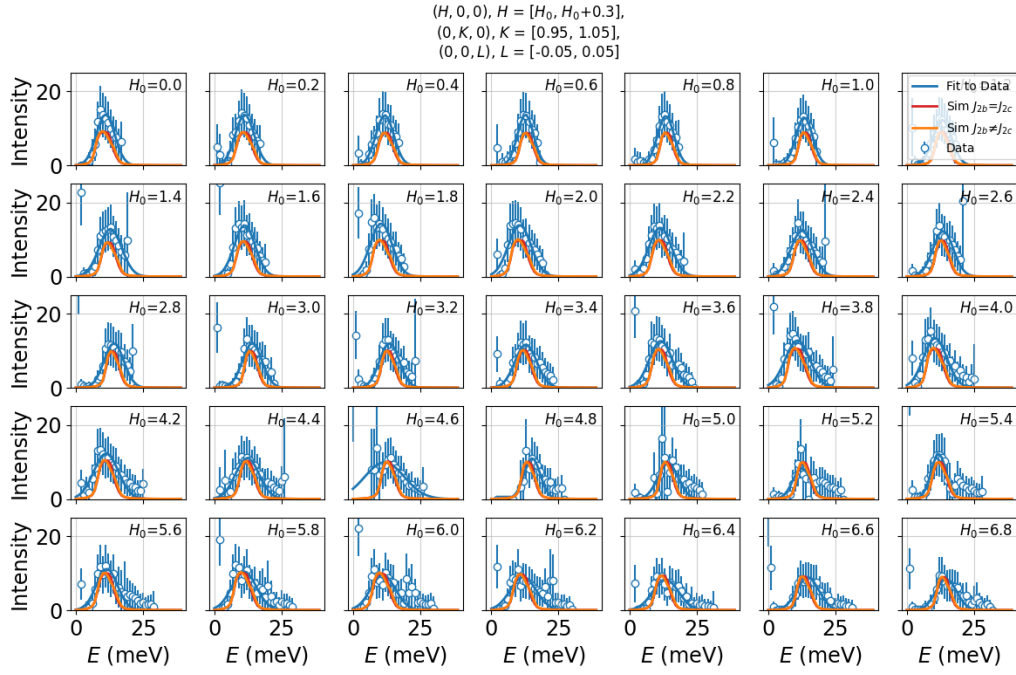


FIG. S4. Cuts of inelastic neutron scattering along $(H, 1, 0)$ made using the integration ranges indicated. Lines show fits using Gaussian functions and simulations using the two model Hamiltonians discussed in the text.